Inorganic Chemistry

pubs.acs.org/IC

Article

Self-Sacrificing Template of the POMs-Based Composite for the High-Performance Organic–Inorganic Hybrid Cathode of Lithium-Ion Batteries

Feng-Cui Shen,*[,§] Can Guo,[§] Sheng-Nan Sun, Zhen Lei, and Ya-Qian Lan*

Cite This: *Inorg. Chem.* 2022, 61, 11182–11188

Read Online

ACCESS | Metrics & More | Article Recommendations | Supporting Information

ABSTRACT: The high theoretical capacity of vanadium oxides makes them promising cathode candidates for the rechargeable lithium-ion batteries (LIBs). Nevertheless, the relatively poor electrical conductivity and capacity retention hinder the practical application and have to be overcome urgently for the increasing demand for storage technologies. Herein, a new BRG system composed of bimetallic oxide/rhodamine B (RB)/reduced graphene oxide (RGO) was prepared through the facile self-sacrificing template of the precursor polyoxometalate (POM) composites POMs/RB/RGO (PRG). RB not only acts as a cationic mediator to facilitate the loading of POMs on graphene for conversion to oxides but also promotes the formation of uniform nanorods on the RGO. The prepared composite FeV_3O_8-RB/RGO-1 as the cathode exhibits superior cycling stability (specific capacity of 225 mA h g^{-1} at 100 mA g^{-1}) and elastic rate capabilities for LIBs. What is more, the new PRG precursor provides versatile possibilities for the design of oxide composites from the self-sacrificing template of POMs-based composites with abundant architectural designs and compositions for the energy storage system.

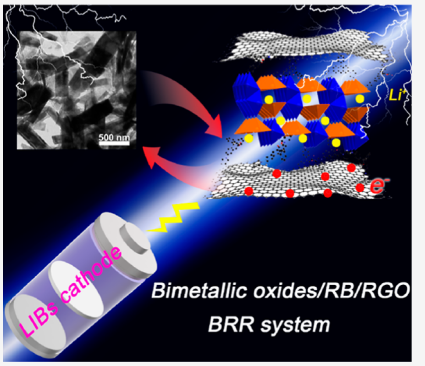

INTRODUCTION

The primer electric energy storage devices of next-generation lithium-ion batteries (LIBs) are important approaches to meet the energy needs and environmental issues.[1,2] Especially, the larger-scale applications of electrified vehicles, hybrid electric vehicles, and smart electronic devices have spurred the burgeon of LIBs with a long cycling life span, high energy density, and good elastic rate capability.[3] However, the major obstacle of the progress is the unsatisfactory performance of cathode materials.[4] Generally speaking, the rapid capacity fading and inferior rate capability depend largely on the intrinsic properties of electrodes.[5] The sustainable progress of next-generation LIBs depends on the intensive research efforts for sustainable redox stability, environmental friendliness, and structural diversity of cathode materials.[6]

Despite the promising lithium-ion storage of vanadium oxides as the attractive cathode candidate for the outstanding high capacity and abundant resources,[7,8] the poor electronic conductivity of vanadium oxide sacrificed the corresponding high capacity advantage.[9] Theoretical calculation and research[10,11] confirmed that polyoxometalates (POMs) as a class of attractive metal-oxo clusters are the outstanding candidates for the distinguished electrodes owing to their tunable compositions, distinctive electron sponge properties, and reversible electrochemical redox features.[12−14] Furthermore, the conversion of polyoxovanadates to vanadium oxides achieves a portable method for accurate synthesis and enrichment of a variety of vanadium oxides with different morphologies and nanostructures,[15] but there are few reports. Especially, some vanadium oxides have the perovskite-like cavities where the metal cations are prone to be displaced by the lithium ion or other cations.[16] Therefore, polyoxovanadates are considered to be ideal precursors for target metal oxide composites by various synthesis methods. However, good solubility in organic electrolytes, poor conductivity, and the aggregation of POMs greatly restrict its scope of application in LIBs.[17,18] Aiming to settle these bottleneck issues, various strategies have been proposed, including compounding with carbon materials,[19,20] ionic liquids,[21] and optimization of the electronic structure.[20] Thus, the judicious design is the self-assembly of POMs to form POM-based composites.[22,23] The layered graphene oxide (GO) emerged as a perfect nanocomposite carrier with a large surface area exposing active sites and interconnected channels as fast charge and mass conductive pathways.[24] However, it also faces challenges from the low loading of POMs on GO due to the electronegativity of both anion clusters and GO.[21] Organic electrodes provide an application potential for sustainable LIBs due to their low cost and flexible architectural characteristics.[25]

Received: April 6, 2022
Published: July 7, 2022

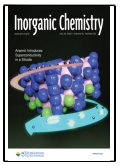

https://doi.org/10.1021/acs.inorgchem.2c01154
Inorg. Chem. 2022, 61, 11182−11188

Dyes as the transitional metal chalcogenides are superior to many materials due to their large intermediate layers.[26,27] Cationic dyes such as rhodamine B (RB) are an outstanding intermediate, and the strong interaction of dyes and POMs[28,29] not only promotes the loading of POMs to form organic−inorganic hybrid materials inspired by the electrostatic interaction but also enables them to act as active sites for lithium-ion storage.

Herein, an organic−inorganic hybrid composite was prepared by the self-assembly of POMs, RB, and reduced GO (RGO) for the first time. In this system, three-dimensional (3D) framework structures $[Fe_3V_{18}O_{42}(H_2O)_{12}(VO_4)]\cdot 24H_2O$ and $[Co_3V_{18}O_{42}(H_2O)_{12}(SO_4)]\cdot 24H_2O$, denoted as Fe_3V_{19} and Co_3V_{18}, respectively,[30] were adopted as the precursor due to the distinguishing multi-electron transfer characteristics and abundant vanadium donors. What is more, they offer a theoretical model for an explicit sharp contrast between distinct transition metal precursors in regard to the properties of the cathode. Not only does RB act as the positive bridge of POMs and GO, but its carboxylic acid group and nitrogen atoms facilitate the intercalation of lithium as well. In addition, the stable $\pi-\pi$ interactions forced the aromatic rings of RB to be directionally distributed on the surface of GO sheets to form the well-defined morphology, which not only effectively improved the loading of the active component but also ensured the rapid transmission of electrons. Also, as all we know, no research has reported a general pathway for the application of the hybrid materials POM−dye as the precursor for LIBs. The as-prepared BRG composites presented outstanding electrochemical storage performances. Especially, the FeV_3O_8-RB/RGO-1 electrode obtained exceptional specific capacity and surprising rate capability. Notably, we have confirmed for the first time that POMs can be used as the sacrificing precursor to guide the formation of an organic−inorganic hybrid. This facile and elaborate design can also offer an original way to develop the exceedingly superior electrode material.

METHODS

Synthesis of BRG Composites. *Synthesis of Polyoxovanadates Fe_3V_{19} and Co_3V_{18}.* Fe_3V_{19} and Co_3V_{18} were prepared using similar methods. First, V_2O_5 (0.03 mol, 5.4564 g) was dissolved in 160 mL of purified water to form an aqueous solution and heated slowly to 85 °C, and then, 36 mL of $LiOH\cdot H_2O$ solution (0.06 mol, 2.5176 g) and $(N_2H_5)_2SO_4$ (0.03 mol, 3.9036 g) were added successively and stirred for 10 min. Then, 2 M HCl was dropped into the solution to adjust the pH to 4.6 after diluting the mixed solution to 300 mL. Next, $FeSO_4\cdot 7H_2O$ (0.015 mol, 4.1703 g) or $CoSO_4\cdot 7H_2O$ (0.015 mol, 4.2172 g) was mixed into the above solution with magnetic stirring for 5 h. After allowing the solution to stand overnight, the resultant black crystals Fe_3V_{19} and Co_3V_{18} were acquired by pressure filtration of the solution.

Synthesis of FeV_3O_8-RB/RGO-1,2,3,4,5 and CoV_3O_8-RB/RGO Composites. First, the procedure of preparing GO was followed effectively according to the modified Hummer's method. Then, GO was ultrasonically dispersed in purified water (2 mg mL^{-1}) for 30 min. 0.252 g of Fe_3V_{19} and 0.02 g of RB were dissolved in the well-dispersed solution and added to the autoclave at 180 °C for 24 h. The as-prepared FeV_3O_8-RB/RGO-1 composite was acquired by vacuum filtration followed by washing with purified water and drying in the vacuum-drying oven. According to the above approach, FeV_3O_8-RB/RGO-2, 3 composites were prepared similar to FeV_3O_8-RB/RGO-1 by altering the loading concentration of GO to 1 and 3 mg mL^{-1}, respectively. FeV_3O_8-RB/RGO-4, 5 were synthesized similarly to FeV_3O_8-RB/RGO-1 with the RB amounts of 0.01 and 0.03 g, respectively. CoV_3O_8-RB/RGO was prepared parallelly to FeV_3O_8-RB/RGO-1 using Co_3V_{18} as the precursor.

Synthesis of FeV_3O_8/RGO and FeV_3O_8-RB. FeV_3O_8/RGO and FeV_3O_8-RB were also prepared similarly to FeV_3O_8-RB/RGO-1 without the addition of RB and GO, respectively.

Materials Characterization. X-ray diffraction (XRD) analysis of D/max-2500/PC (Rigaku) was carried out to collect the powder XRD data using graphite monochromatized Cu Kα radiation. The surface morphologies of composites were detected using the JSM-7600 F apparatus for scanning electron microscopy (SEM) at an acceleration voltage of 10 kV. The JEOL-2100 F equipment with an acceleration voltage of 200 kV was used to obtain the transmission electron microscopy (TEM) images. The elemental composition and corresponding elemental mapping of various composites were detected by energy-dispersive X-ray spectroscopy (EDS, JSM-5160LV). The Raman spectrum was obtained on the Renishaw 1000 spectrometer equipped with a 514.5 nm Arion laser. A Shimadzu-60 thermo-analyzer was used for the thermogravimetric analysis (TGA) in the range from room temperature to 1100 °C with a heating rate of 10 °C min^{-1} under an air atmosphere. The Brunauer−Emmett−Teller (BET) surface area and nitrogen adsorption−desorption isotherms were measured at 77 K on a Quantachrome Instruments Autosorb AS-6B. The Barrett−Joyner−Halenda (BJH) model was used to calculate the relative pore size distributions. X-ray photoelectron spectroscopy (XPS) was performed on the scanning X-ray microprobe using Al kα radiation with the standard binding energy of the C 1s peak at 284.8 eV.

Electrochemical Measurements. For LIB fabrication, the cathode was prepared by mixed grinding of active nanocomposites, super P carbon black, and polyvinylidene fluoride with a weight ratio of 7:2:1. Then, the formed slurries were coated on glossy aluminum foil homogeneously and dried in a vacuum oven at 90 °C for 12 h. The assembly of coin-type cells was performed in the argon-filled glovebox with a low content of water and oxygen components. The Celgard 2400 and Li metal acted as the separator and anode, respectively, in the assembled 2032-type half cells. The electrolyte was composed of the same volumes of dimethyl carbonate, ethyl methyl carbonate, and ethylene carbonate with 1 M $LiPF_6$. Then, the electrochemical properties were measured on the Land CT2001A battery measurement platform in a voltage window of 1.5−3.5 V after aging the cells for 12 h at room temperature. Cyclic voltammetry (CV) measurement was conducted on a CHI660e between 1.5 and 3.5 V at the scan rate of 0.02 mV s^{-1}. Electrochemical impedance spectroscopy (EIS) was performed on CHI660e under the open-circuit potential, with an AC amplitude of 5 mV and a frequency range of 100 kHz −0.01 Hz.

RESULTS AND DISCUSSION

Electrode Material Synthesis and Physical Characterization. The synthesis of composite FeV_3O_8-RB/RGO-1 is illustrated concretely in Figure 1 by a one-pot hydrothermal method adopting Fe_3V_{19} (Figure S1), dye, and GO as precursors. Upon the hydrothermal treatment, cationic dye RB serves as the "holder" molecule anchored on the electronegativity of GO nanosheets for the appropriate space to load the POMs. Fe_3V_{19} not only serves as the precursor of FeV_3O_8 but is also used as the reductive agent for GO.

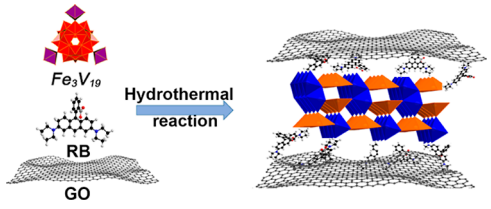

Figure 1. Schematic diagram of the synthesis of composite FeV_3O_8-RB/RGO-1.

https://doi.org/10.1021/acs.inorgchem.2c01154
Inorg. Chem. 2022, 61, 11182−11188

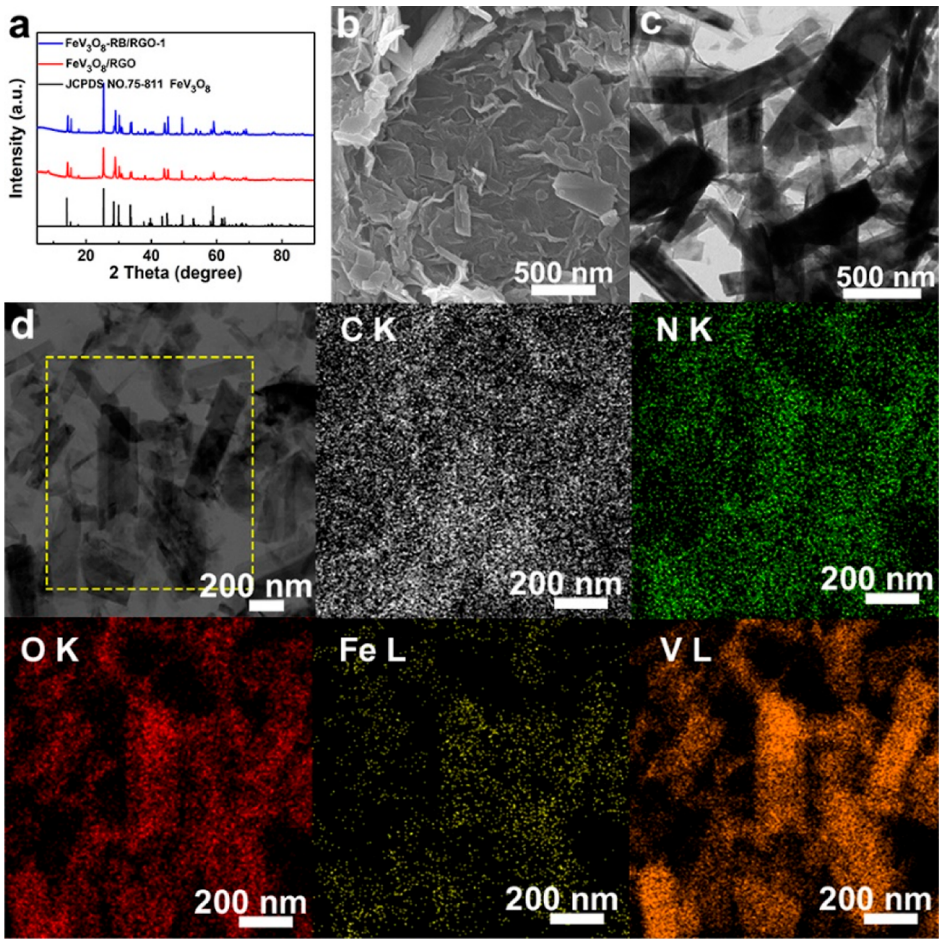

Figure 2. Characterizations of the controlled composites. (a) XRD patterns of FeV_3O_8-RB/RGO-1 and FeV_3O_8/RGO. (b–d) SEM, TEM, and EDS elemental mapping images of FeV_3O_8-RB/RGO-1.

As a control experiment, FeV_3O_8-RB/RGO-1 composites without the addition of GO or RB, denoted as FeV_3O_8-RB and FeV_3O_8/RGO, were also synthesized. To understand the influence of GO concentration on lithium-ion storage capacity, the composites obtained with the concentrations of GO of 1 and 3 mg mL^{-1} were used in the procedure, labeled as FeV_3O_8-RB/RGO-2 and FeV_3O_8-RB/RGO-3, respectively. Furthermore, to explore the effect of the POMs on electrode properties, we employed $Co_3V_{18}O_{42}(H_2O)_{12}(SO_4)\cdot 24\ H_2O$ (Co_3V_{18}) with the same crystal structure as that of Fe_3V_{19} (Figure S1a) as the precursor, whose composite was denoted as CoV_3O_8-RB/RGO. XRD measurements (Figure 2a) were performed for the structural characterization of the synthesized samples. As can be seen, they exhibit almost identical highly crystalline diffraction peaks as those indexed as FeV_3O_8 corresponding to JCPDS no 75-811. The morphologies of the related synthetic composites were characterized by SEM. Obviously, FeV_3O_8-RB nanorods were stacked together (Figure S2a) in the absence of RGO under the action of van der Waals forces, resulting in a small specific surface to contact the electrolyte. Interestingly, when GO was introduced into the system, FeV_3O_8-RB/RGO displayed the uniform distribution of FeV_3O_8-RB sheets grown on RGO without evidently cumulating in bulk on the RGO for the strong intermolecular $\pi-\pi$ interactions of RB and RGO as Figure 2b,c, reflecting the effectiveness of self-assembly between the complicated system. The homogeneous morphology of FeV_3O_8/RGO was observed with a typical multilayer and close-packed morphology of RGO under the absence of RB (Figure S3a). When Fe_3V_{19} was replaced by Co_3V_{18} in the procedure of FeV_3O_8-RB/RGO, analogous nanorod structures of CoV_3O_8-RB/RGO, as shown in Figure S4a, were obtained, which may be attributed to the conjugation of key medium cationic RB.

Their microstructures were further investigated by TEM. Note that FeV_3O_8-RB (Figure S2b) tended to densely stack together without RGO insertion, which greatly diminished the accessible active sites for the electrolyte. The weak interaction between anion clusters of POMs and electronegative RGO in the precursor led to the stacking sheet distribution in FeV_3O_8/RGO (Figure S3b). However, FeV_3O_8-RB/RGO and CoV_3O_8-RB-RGO exhibited the well-distributed morphology of staggered sheets on RGO, as shown in Figures 2c and S4b, which hence shortened the diffusion length for electrons and lithium ions simultaneously. The uniformity of composites synthesized by the hydrothermal method was further confirmed by elemental mapping images. As shown in Figures 2d and S2c, S3c, and S4c, all the elements were evenly distributed in the composites at the nanoscale. Especially, the element of N was observed in the composites in accordance with the EDS spectrum (Figure S5), which fully testified to the successful integration of RB.

As presented in Figure S6a, the characteristic peaks in Raman spectra showed the presence of GO, RB, and oxide FeV_3O_8, respectively. RGO exhibited the emergence of two

https://doi.org/10.1021/acs.inorgchem.2c01154
Inorg. Chem. 2022, 61, 11182–11188

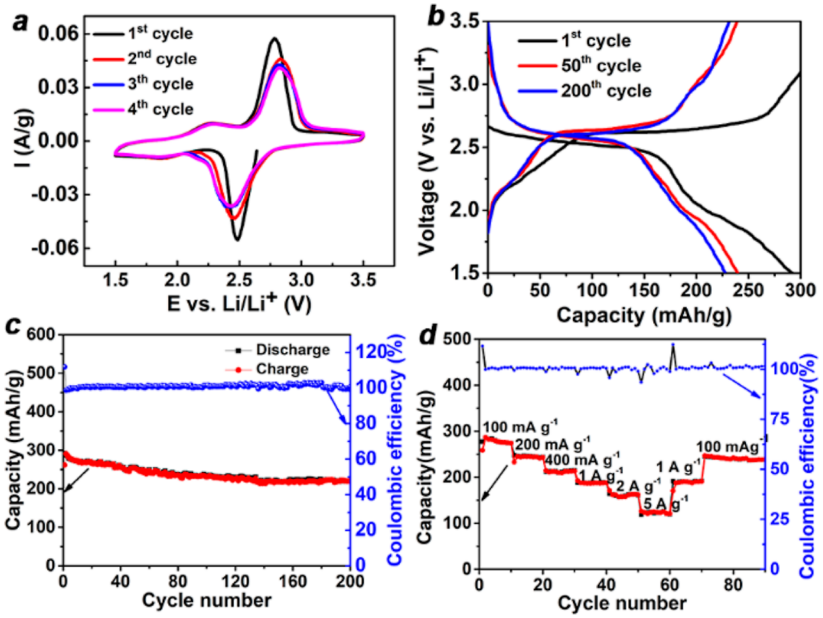

Figure 3. Electrochemical properties of the FeV_3O_8-RB/RGO-1 composite. (a) CV profiles of FeV_3O_8-RB/RGO-1 at a sweep speed of 0.2 mV s^{-1} in a 2032 coin-type cell. (b,c) Charging and discharging profiles and cycling performance of FeV_3O_8-RB/RGO-1 at 100 mA g^{-1}. (d) Rate capability of FeV_3O_8-RB/RGO-1 under diverse current densities.

classic peaks located at 1353 cm^{-1} (D band) and 1593 cm^{-1} (G band). The signal peaks of FeV_3O_8/RGO observed at 200−300 and 645 cm^{-1} were related to the nonequivalent and stretching vibrations of Fe−O. Signal peaks of 350−500 and 820 cm^{-1} were assigned to the stretching bands of V−O−V and V−O−e, respectively.[31,32] The Raman spectrum region at around 619 cm^{-1} was attributed to the xanthene ring puckering bonds, while the region from 1195 to 1644 cm^{-1} in the spectrum was assigned to C−C, C−H, and C═C stretching of RB in RB/RGO and FeV_3O_8-RB/RGO.[33,34] TGA tests for FeV_3O_8/RGO and FeV_3O_8-RB/RGO were performed, as shown in Figure S6b. The weight loss values of about 5 and 7% at 270 and 395 °C in FeV_3O_8/RGO, respectively, were related to the absence of the crystal water and the carbonization of RGO. When the temperature was increased further, the weight increased a little, which may be ascribed to the oxidation of low-valence V^{3+} and V^{4+} of FeV_3O_8 under the oxygen atmosphere at high temperature, and finally tended to stabilize. Simultaneously, the weight loss of 12% in FeV_3O_8-RB/RGO resulted from the removal of the crystal water and RB and the carbonization of RGO. Notably, when the temperature exceeded 400 °C, the thermogravimetric mass had a significant increase compared with that of FeV_3O_8/RGO, indicating the improved loading of FeV_3O_8 in the system of FeV_3O_8-RB/RGO. The BET surface area of FeV_3O_8-RB/RGO was characterized to be 87 m^2 g^{-1} by nitrogen sorption isotherms, which was nearly twice that of FeV_3O_8/RGO of 44.5 m^2 g^{-1} (Figure S6c) due to the support of RGO by RB. The large specific surface area of FeV_3O_8-RB/RGO-1 manifested a significant potential for electrochemical application. The corresponding pore size distribution of FeV_3O_8-RB/RGO was calculated to be a mesoporous diameter of around 4 nm, similar to that of FeV_3O_8/RGO calculated by the BJH method (Figure S6d).

XPS analysis was performed to identify the valence of FeV_3O_8-RB/RGO-1 before and after Li insertion, as shown in Figure S7, which fully demonstrated the signals of C, Fe, and V. The C 1s spectrum of nanocomposite FeV_3O_8-RB/RGO-1 (Figure S7a) had a relatively strong peak located at 284.6 eV for C═C and three relatively weak peaks located at 285.4 for C−C, 286.4 for C−N/C−O, and 288.4 eV for C═O,[35,36] which further manifested the RB doping and formation of RGO in the synthetic process. After charging to 3.5 V, C═O turned into C−O for the Li insertion, as shown in Figure S7b. The Fe 2p spectrum displayed two characteristic peaks associated to Fe $2p_{1/2}$ (710.2 eV) and Fe $2p_{3/2}$ (725.1 eV) of Fe^{3+} before and after charging to 3.5 V.[37,38] The presented binding energies of 516.7, 517.6, 523.5, and 524.8 eV in the V 2p spectrum were assigned to the typical peaks of V $2p_{1/2}$ and V $2p_{3/2}$ originating from V^{4+} and V^{5+} of FeV_3O_8.[21] Remarkably, the emerging characteristic peaks were attributed to V $2p_{1/2}$ (515.8 eV) and V $2p_{3/2}$ (522.9 eV) of V^{3+} for the intercalation reaction after charging to 3.5 V.[38]

The lithium-ion storage performance of the FeV_3O_8-RB/RGO-1 composite was first evaluated by CV measurements using a 2032 coin-type cell. The first four consecutive CV profiles are presented in Figure 3a, including the multi-step redox process. The peaks at 2.47 and 2.1 V and at 2.25 and 2.8 V can be viewed during the reduction and oxidation curves in the first cycle. The first obvious reduction peak located at 2.47 V was attributed to the insertion of lithium into the oxide FeV_3O_8 ($Fe^{3+}V_1^{5+}V_2^{4+}O_8$), forming $Li_xFe^{3+}V_{1-x}^{5+}V_{2+x}^{4+}O_8$ corresponding to the reduction of $V^{5+}(3d^0)$ to $V^{4+}(3d^1)$. The weak reduction peak located at 2.1 V was consistent with the discharge platform of Figure 3b and was attributed to parts of $Li_xFe^{3+}V_{1-x}^{5+}V_{2+x}^{4+}O_8$ reducing to $Li_xFe^{3+}V_{3-(x-1)}^{4+}V_{x-1}^{3+}O_8$ corresponding to the reduction of V^{4+} ($3d^1$) to V^{3+} ($3d^2$), leading to the lower discharge plateau of the first cycle than that of the latter cycles. Similarly, the oxidation peaks at 2.25 and 2.8 V could be resulted from the oxidation of V^{3+} to V^{4+} and V^{4+} to V^{5+}, respectively. During the subsequent cycles, the tiny voltage changes of the redox reaction could be due to the strain and structural changes during the initial electrochemical process.[39] Their current densities and integral areas of the

https://doi.org/10.1021/acs.inorgchem.2c01154
Inorg. Chem. 2022, 61, 11182−11188

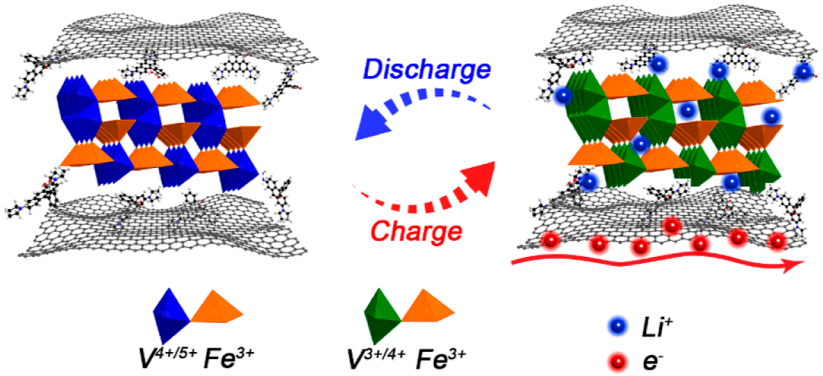

Figure 4. Schematic diagram of the possible storage mechanism for the FeV_3O_8-RB/RGO-1 electrode.

redox peaks are basically similar, indicating the good reversibility of redox reactions for the lithiation and delithiation processes.[40]

Charging and discharging profiles are depicted in Figure 3b in the voltage range of 1.5−3.5 V at 100 mA g^{-1}. The charge−discharge wide voltage plateaus may be induced by the multistep reaction process,[27] which were generally consistent with the above CV curves. Evidently, the narrow gaps between the discharge and charge voltage plateaus manifested the inferior degree of polarization, which further ensured the stability of the cycling as a cathode. The initial discharge capacity of FeV_3O_8-RB/RGO reached up to 292.4 mA h g^{-1}. The subsequent capacity loss may be ascribed to the reaction of the lithium ions with the oxygenic functional group on RGO, which is very common for electrode composites.[41,42] A galvanostatic cycling investigation was carried out to confirm the cycling stability performance of the FeV_3O_8-RB/RGO-1 composite at 100 mA g^{-1}. The reversible capacities of 250 and 225 mA h g^{-1} were obtained after 100 and 200 cycles (only 0.11% loss per cycle for 200 cycles), respectively, as shown in Figure 3c, which remained stable after cycling, indicating the high reversibility of lithiation and delithiation. The rate capability as the crucial characteristic of the electrodes was tested at diverse current densities, as shown in Figure 3d, and FeV_3O_8-RB/RGO-1 exhibited a remarkable rate capability as well due to its unique architecture. The discharge capacities obtained were 250, 150, and 120 mA h g^{-1} at 100, 2000, and 5000 mA g^{-1}, respectively. Furthermore, the capacity can be fully recovered after the high current cycling when the current was reset to a low rate. More remarkably, the FeV_3O_8-RB/RGO-1 electrode exhibited superior cycling performance at large current density. A high capacity of 150 mA h g^{-1} was acquired with only 0.17% capacity loss for 500 cycles even at 2000 mA g^{-1} (Figure S8a). As is known, the excellent resilience is vital for high-quality electrodes, and such an excellent rate shows the great potential of the promising alternative cathode for LIBs.

To clarify the effect of different compositions on lithium-ion storage performances, the controlled composites prepared without RB or GO were labeled as FeV_3O_8/RGO and FeV_3O_8-RB, respectively. Compared with FeV_3O_8-RB/RGO-1, although the FeV_3O_8/RGO composite exhibited a stable cycling ability, it only showed a lower capacity of 118 mA h g^{-1} at the 100th cycle at 100 mA g^{-1}, as shown in Figure S8b,c, manifesting that RB doping can introduce the activity site for coordination with lithium ions and increase the interlayer spacing of RGO for integrating more POM (Fe_3V_{19}) precursor. The homogeneous distribution of FeV_3O_8-RB on RGO is conducive to the transmission of lithium ions and electrons, improving its electrochemical performance. Furthermore, the carboxylic acid group and nitrogen atoms of RB also facilitate the coordination with lithium and thus contribute to capacity. However, FeV_3O_8-RB acquired the lowest capacity of 37 mA h g^{-1}, fully proving the influence of conductivity and the effect of the spatial structure of aggregated sheets on electrode electrochemical performance. The relationship between GO concentration and electrochemical performance was further researched, as shown in Figure S8d, and composites FeV_3O_8-RB/RGO-2 and FeV_3O_8-RB/RGO-3 with the concentration of GO 1 and 3 mg mL^{-1}, respectively, were prepared for comparison. Comparatively speaking, the inferior performance of FeV_3O_8-RB/RGO-2 and FeV_3O_8-RB/RGO-3 illustrated the significant influence of GO concentration. Although the low concentration of GO improved the electrical conductivity of composites to a certain extent, it cannot prevent FeV_3O_8-RB nanorods from agglomerating while cycling. However, a high concentration of GO may lead to less active material FeV_3O_8-RB encapsulated by RGO not conveniently in contact with the electrolyte. To investigate the influence of the amount of RB on the capacity, FeV_3O_8-RB/RGO-4 and FeV_3O_8-RB/RGO-5 were also synthesized and applied as the cathodes of LIBs. Their electrochemical performance was researched, and the poor performance observed is shown in Figure S8e. The low quality of RB may lead to the low content of the formed active components FeV_3O_8-RB on RGO. In contrast, the high quality of RB may induce poor conductivity.

This facile self-sacrificing template approach is also successfully applied to other polyoxovanadates. Co_3V_{18} having similar structural units to Fe_3V_{19} was opted to prepare CoV_3O_8-RB/RGO, enriching the BRG system. Significantly, composite CoV_3O_8-RB/RGO has a similar morphology to FeV_3O_8-RB/RGO-1 (Figure S4), which may be due to the conjugation between the aromatic ring of RB and the benzene ring of RGO guiding the formation of the morphology. The CoV_3O_8-RB/RGO composite was applied as the cathode to compare different polyoxovanadates in terms of the lithium-ion storage performance, as shown in Figure S9. Interestingly, the capacity of only 180 mA h g^{-1} was obtained at 100 mA g^{-1} after 100 cycles. Furthermore, specific capacities of about 95 and 168 mA h g^{-1} were acquired at 2000 and 5000 mA g^{-1}, respectively. The poor electrochemical performance of CoV_3O_8-RB/RGO may be due to the lower atomic ratio of V/Co in Co_3V_{18} than that of V/Fe in Fe_3V_{19}. One vanadium atom less in a unit molecular of Co_3V_{18} may lead to less active

https://doi.org/10.1021/acs.inorgchem.2c01154
Inorg. Chem. 2022, 61, 11182−11188

sites, resulting in the poor capacity and rate capability of CoV_3O_8-RB/RGO.

To provide insights into the kinetics for lithium ions insertion/extraction in FeV_3O_8-RB/RGO-1 and FeV_3O_8/RGO, the EIS measurements were carried out. Nyquist plots (Figure S10) revealed obvious semicircles and inclined lines with a slope of about 45° in the range of high-to-medium frequencies and the low-frequency range, which corresponds to the charge transfer resistance (Rct) and lithium-ion diffusion resistance, respectively. The smaller resistance of FeV_3O_8-RB/RGO-1(266 Ω) than that of FeV_3O_8/RGO (442 Ω) indicates the faster reaction kinetics for lithium-ion insertion and extraction, attributed to the fact that the conjugated behavior between the aromatic ring of RB and the benzene ring of RGO is more conducive to the transmission of electrons in the system.

FeV_3O_8-RB/RGO-1 achieving a reasonably good stability and robust rate capability as the cathode should be closely related to its unique compositions. The possible storage mechanism of the FeV_3O_8-RB/RGO-1 composite is illustrated in Figure 4. First, organic−inorganic composites endow abundant redox-active sites for lithium ions access. Second, the conductive network RGO sheets facilitate fast charge and electron transport to stimulate the lithium ions intercalation reaction in a cell, thus shortening the lithium ions diffusion distance and greatly improve the efficiency of accessible active sites for lithium ions insertion. Third, composite FeV_3O_8-RB nanorods distributed on RGO may have a large inner space for expanding and effectively avoid the volume effect by lithium ions embedding in the active composites. Electrode FeV_3O_8-RB/RGO-1 had a well-conserved morphology after cycling, which evidenced that the cathode has no pulverization without a collapse structure, as shown in Figure S10. All these factors contribute to the high capacity and superior rate capability.

CONCLUSIONS

In conclusion, a simple approach was developed to prepare the BRG system through the positive linker RB bridging heteropolyanion cluster POMs and carbon substrate GO under the action of electrostatic interaction in the precursor, along with in situ reduction of GO and oxidation of POMs in the hydrothermal process. This elaborate self-sacrificing template of PRG system endows the BRG electrodes with unique features, combining the electronic donor of the organic−inorganic hybrid and the electron conductive buffering framework. FeV_3O_8-RB/rGO-1 manifests a promising performance as a cathode for LIB with high capacity and outstanding rate capability. This work highlights the facile self-sacrificing template approach based on POMs for oxide composites serving as ideal candidates for the cathode of LIBs.

ASSOCIATED CONTENT

Supporting Information

The Supporting Information is available free of charge at https://pubs.acs.org/doi/10.1021/acs.inorgchem.2c01154.

Related electrode characterizations and electrochemical performances (PDF)

AUTHOR INFORMATION

Corresponding Authors

Feng-Cui Shen − *School of Chemical and Environmental Engineering, Anhui Polytechnic University, Wuhu 241000, China;* orcid.org/0000-0002-7100-6261; Email: fcshen@ahpu.edu.cn

Ya-Qian Lan − *School of Chemistry, South China Normal University, Guangzhou 510006, China;* orcid.org/0000-0002-2140-7980; Email: yqlan@njnu.edu.cn

Authors

Can Guo − *School of Chemistry, South China Normal University, Guangzhou 510006, China*

Sheng-Nan Sun − *School of Chemistry, South China Normal University, Guangzhou 510006, China*

Zhen Lei − *School of Chemical and Environmental Engineering, Anhui Polytechnic University, Wuhu 241000, China*

Complete contact information is available at: https://pubs.acs.org/10.1021/acs.inorgchem.2c01154

Author Contributions

§F.-C.S. and C.G. contributed equally to this work.

Notes

The authors declare no competing financial interest.

ACKNOWLEDGMENTS

This work was supported financially by the National Natural Science Foundation of China (no 21901003), Anhui Provincial Department of Education (no KJ2019A0139), and Key Laboratory Open Foundation of Anhui Province (no LCECSC-09).

REFERENCES

(1) Li, W.; Song, B.; Manthiram, A. High-voltage positive electrode materials for lithium-ion batteries. *Chem. Soc. Rev.* **2017**, *46*, 3006−3059.

(2) Zheng, J.; Lu, J.; Amine, K.; Pan, F. Depolarization effect to enhance the performance of lithium ions batteries. *Nano Energy* **2017**, *33*, 497−507.

(3) Lee, J. W.; Lim, S. Y.; Jeong, H. M.; Hwang, T. H.; Kang, J. K.; Choi, J. W. Extremely stable cycling of ultra-thin V_2O_5 nanowire-graphene electrodes for lithium rechargeable battery cathodes. *Energy Environ. Sci.* **2012**, *5*, 9889−9894.

(4) Rodriguez, R.; Deiner, L. J.; Tsao, B. H.; Fellner, J. P. Aerosol jet-printed LFP cathodes with bimodal pore distribution improve the rate capability of LIB cells. *ACS Appl. Energy Mater.* **2021**, *4*, 9507−9512.

(5) Zhang, J.; Ren, H.; Wang, J.; Qi, J.; Yu, R.; Wang, D.; Liu, Y. Engineering of multi-shelled SnO_2 hollow microspheres for highly stable lithium-ion batteries. *J. Mater. Chem. A* **2016**, *4*, 17673−17677.

(6) Tao, Y.; Rahn, C. D.; Archer, L. A.; You, F. Second life and recycling: energy and environmental sustainability perspectives for high-performance lithium-ion batteries. *Sci. Adv.* **2021**, *7*, No. eabi7633.

(7) Zhou, R.; Li, X.; Pang, H. VOx/VSx@Graphene nanocomposites for electrochemical energy storage. *Chem. Eng. J.* **2021**, *404*, 126310.

(8) Wu, C.; Xie, Y. Promising vanadium oxide and hydroxide nanostructures: from energy storage to energy saving. *Energy Environ. Sci.* **2010**, *3*, 1191−1206.

(9) Yao, X.; Guo, G.; Li, P.-Z.; Luo, Z.-Z.; Yan, Q.; Zhao, Y. Scalable synthesis of honeycomblike V_2O_5/carbon nanotube networks as enhanced cathodes for lithium-ion batteries. *ACS Appl. Mater. Interfaces* **2017**, *9*, 42438−42443.

(10) Wang, H.; Hamanaka, S.; Nishimoto, Y.; Irle, S.; Yokoyama, T.; Yoshikawa, H.; Awaga, K. In operand X-ray absorption fine structure studies of polyoxometalate molecular cluster batteries: polyoxometalates as electron sponges. *J. Am. Chem. Soc.* **2013**, *134*, 4918−4924.

(11) Chen, J.-J.; Symes, M. D.; Fan, S.-C.; Zheng, M.-S.; Miras, H. N.; Dong, Q.-F.; Cronin, L. High-performance polyoxometalate-based

cathode materials for rechargeable lithium-ion batteries. *Adv. Mater.* **2015**, *27*, 4649−4654.
(12) Huang, S.-C.; Lin, C.-C.; Hsu, C.-T.; Guo, C.-H.; Chen, T.-Y.; Liao, Y.-F.; Chen, H.-Y. Keplerate-type polyoxometalate $\{Mo_{72}Fe_{30}\}$ nanoparticle anodes for high-energy lithium-ion batteries. *J. Mater. Chem. A* **2020**, *8*, 21623−21633.
(13) Liu, J.; Chen, Z.; Chen, S.; Zhang, B.; Wang, J.; Wang, H.; Tian, B.; Chen, M.; Fan, X.; Huang, Y.; Sum, T. C.; Lin, J.; Shen, Z. X.; Shen, Z. X. Electron/ion sponge"-like V-based polyoxometalate: toward high-performance cathode for rechargeable sodium ion batteries. *ACS Nano* **2017**, *11*, 6911−6920.
(14) Li, M.-T.; Yang, X.-Y.; Li, J.-S.; Sheng, N.; Liu, G.-D.; Sha, J.-Q.; Lan, Y.-Q. Assembly of multifold helical polyoxometalate-based metal−organic frameworks as anode materials in lithium-ion batteries. *Inorg. Chem.* **2018**, *57*, 3865−3872.
(15) Bayaguud, A.; Zhang, Z.; Geng, M.; Fu, Y.; Yu, Y.; Zhu, C. Transformation of polyoxometalate into 3D porous Li-containing oxide: a case study of gamma-LiV_2O_5 for high-performance cathodes of Li-ion batteries. *Small Methods* **2019**, *3*, 1900187.
(16) Cava, R. J.; Santoro, A.; Murphy, D. W.; Zahurak, S.; Roth, R. S. The structures of lithium inserted metal oxides: $Li_2FeV_3O_8$. *J. Solid State Chem.* **1983**, *48*, 309−317.
(17) Li, M.; Cong, L.; Zhao, J.; Zheng, T.; Tian, R.; Sha, J.; Su, Z.; Wang, X. Self-organization towards complex multi-fold meso-helices in the structures of Wells-Dawson polyoxometalate-based hybrid materials for lithium-ion batteries. *J. Mater. Chem. A* **2017**, *5*, 3371−3376.
(18) Jia, X.; Wang, J.; Hu, H.; Song, Y. F. Three-dimensional carbon framework anchored polyoxometalate as a high-performance anode for lithium-ion batteries. *Chem. - Eur. J.* **2020**, *26*, 5257−5263.
(19) Hu, J.; Ji, Y.; Chen, W.; Streb, C.; Song, Y.-F. "Wiring" redox-active polyoxometalates to carbon nanotubes using a sonication-driven periodic functionalization strategy. *Energy Environ. Sci.* **2016**, *9*, 1095−1101.
(20) Wang, J.; Liu, Y.; Sha, Q.; Cao, D.; Hu, H.; Shen, T.; He, L.; Song, Y.-F. Electronic Structure reconfiguration of self-supported polyoxometalate-based lithium-ion battery anodes for efficient lithium storage. *ACS Appl. Mater. Interfaces* **2022**, *14*, 1169−1176.
(21) Shen, F.-C.; Wang, Y.-R.; Li, S.-L.; Liu, J.; Dong, L.-Z.; Wei, T.; Cui, Y.-C.; Wu, X. L.; Xu, Y.; Lan, Y.-Q. Self-assembly of polyoxometalate/reduced graphene oxide composites induced by ionic liquids as a high-rate cathode for batteries: "killing two birds with one stone". *J. Mater. Chem. A* **2018**, *6*, 1743−1750.
(22) Chang, J.-N.; Zhang, M.; Gao, G.-K.; Lu, M.; Wang, Y.-R.; Jiang, C.; Li, S.-L.; Chen, Y.; Lan, Y.-Q. Construction of an electron bridge in polyoxometalates/graphene oxide ultrathin nanosheets to boost the lithium storage performance. *Energy Fuels* **2020**, *34*, 16968−16977.
(23) Zhong, Y.; Su, Y.; Huang, P.; Jiang, Q.; Lin, Y.; Wu, H.; Hensen, E. J. M.; Abdelkader, A. M.; Xi, K.; Lai, C.; Chou, S. Polyoxometalate ionic sponge enabled dendrite-free and highly stable lithium metal anode. *Small Methods* **2022**, *6*, 2101613.
(24) Gao, F.; Qin, S.-h.; Zang, Y.-h.; Gu, J.-f.; Qu, J.-y. Highly efficient formation of Mn_3O_4-graphene oxide hybrid aerogels for use as the cathode material of high performance lithium ion batteries. *N. Carbon Mater.* **2020**, *35*, 121−130.
(25) Luo, Z.; Liu, L.; Zhao, Q.; Li, F.; Chen, J. An insoluble benzoquinone-based organic cathode for use in rechargeable lithium-ion batteries. *Angew. Chem., Int. Ed.* **2017**, *56*, 12561−12565.
(26) Lee, J.; Park, M. J. Tattooing dye as a green electrode material for lithium batteries. *Adv. Energy Mater.* **2017**, *7*, 1602279.
(27) Ai, W.; Zhou, W. W.; Du, Z. Z.; Sun, C. C.; Yang, J.; Chen, Y.; Sun, Z. P.; Feng, S.; Zhao, J. F.; Dong, X. C.; Huang, W.; Yu, T. Toward high energy organic cathodes for Li-ion batteries: A case study of vat dye/graphene composites. *Adv. Funct. Mater.* **2017**, *27*, 1603603.
(28) Valley, B.; Jing, B.; Ferreira, M.; Zhu, Y. Rapid and efficient coacervate extraction of cationic industrial dyes from wastewater. *ACS Appl. Mater. Interfaces* **2019**, *11*, 7472−7478.
(29) Yang, H.; Bai, L.; Wei, D.; Yang, L.; Wang, W.; Chen, H.; Niu, Y.; Xue, Z. Ionic self-assembly of poly(ionic liquid)-polyoxometalate hybrids for selective adsorption of anionic dyes. *Chem. Eng. J.* **2019**, *358*, 850−859.
(30) Khan, M. I.; Yohannes, E.; Doedens, R. J. $[M_3V_{18}O_{42}(H_2O)_{12}(XO_4)]\ 24H_2O$ (M: Fe, Co; X: V, S): metal oxide based framework materials composed of polyoxovanadate clusters. *Angew. Chem., Int. Ed.* **1999**, *38*, 1292.
(31) Dutta, D. P.; Ramakrishnan, M.; Roy, M.; Kumar, A. Effect of transition metal doping on the photocatalytic properties of $FeVO_4$ nanoparticles. *J. Photochem. Photobiol., A* **2017**, *335*, 102−111.
(32) Huang, Z.; Tang, X.; Zhao, J.; Lin, H.; Nie, M.; Li, Q. FeV_3O_8/MoS_2 nanostructure heterojunctions as a highly effective electrocatalyst for hydrogen evolution. *J. Mater. Chem. C* **2022**, *10*, 3489−3499.
(33) Lin, S.; Hasi, W.-L. -J.; Lin, X.; Han, S.-q. -g. -w.; Lou, X.-T.; Yang, F.; Lin, D.-Y.; Lu, Z.-W. Rapid and sensitive SERS method for determination of Rhodamine B in chili powder with paper-based substrates. *Anal. Methods* **2015**, *7*, 5289−5294.
(34) Zhang, J.; Li, X.; Sun, X.; Li, Y. Surface enhanced raman scattering effects of silver colloids with different shapes. *J. Phys. Chem. B* **2005**, *109*, 12544−12548.
(35) Tang, Y.-J.; Wang, Y.; Wang, X.-L.; Li, S.-L.; Huang, W.; Dong, L.-Z.; Liu, C.-H.; Li, Y.-F.; Lan, Y.-Q. Molybdenum disulfide/nitrogen-doped reduced graphene oxide nanocomposite with enlarged interlayer spacing for electrocatalytic hydrogen evolution. *Adv. Energy Mater.* **2016**, *6*, 1600116.
(36) Niu, F. E.; Yang, J.; Wang, N. N.; Zhang, D. P.; Fan, W. L.; Yang, J.; Qian, Y. T. $MoSe_2$-covered N,P-doped carbon nanosheets as a long-life and high-rate anode material for sodium-ion batteries. *Adv. Funct. Mater.* **2017**, *27*, 1700522.
(37) Long, C.; Jiang, L.; Wei, T.; Yan, J.; Fan, Z. High-performance asymmetric supercapacitors with lithium intercalation reaction using metal oxide-based composites as electrode materials. *J. Mater. Chem. A* **2014**, *2*, 16678−16686.
(38) Fan, K.; Ji, Y.; Zou, H.; Zhang, J.; Zhu, B.; Chen, H.; Daniel, Q.; Luo, Y.; Yu, J.; Sun, L. Hollow iron-vanadium composite spheres: a highly efficient iron-based water oxidation electrocatalyst without the need for nickel or cobalt. *Angew. Chem., Int. Ed.* **2017**, *56*, 3289−3293.
(39) Wu, C.; Maier, J.; Yu, Y. Generalizable synthesis of metal-sulfides/carbon hybrids with multiscale, hierarchically ordered structures as advanced electrodes for lithium storage. *Adv. Mater.* **2016**, *28*, 174−180.
(40) Li, H.-H.; Zhou, L.; Zhang, L.-L.; Fan, C.-Y.; Fan, H.-H.; Wu, X.-L.; Sun, H.-Z.; Zhang, J.-P. Co_3O_4 nanospheres embedded in a nitrogen-doped carbon framework: an electrode with fast surface-controlled redox kinetics for lithium storage. *ACS Energy Lett.* **2017**, *2*, 52−59.
(41) Han, F.; Li, D.; Li, W.-C.; Lei, C.; Sun, Q.; Lu, A.-H. Nanoengineered polypyrrole-coated Fe_2O_3@C multifunctional composites with an improved cycle stability as lithium-ion anodes. *Adv. Funct. Mater.* **2013**, *23*, 1692−1700.
(42) Yuan, T.; Jiang, Y.; Sun, W.; Xiang, B.; Li, Y.; Yan, M.; Xu, B.; Dou, S. Ever-increasing pseudocapacitance in RGO−MnO−RGO sandwich nanostructures for ultrahigh-rate lithium storage. *Adv. Funct. Mater.* **2016**, *26*, 2198−2206.

https://doi.org/10.1021/acs.inorgchem.2c01154
Inorg. Chem. 2022, 61, 11182−11188